Hemodynamic perturbations due to the presence of stents

Accepted chapter available at https://doi.org/10.1016/C2017-0-03308-6

Hemodynamic perturbations due to the presence of stents

Claudio Chiastra[1,2], Gabriele Dubini[1], Francesco Migliavacca[1]

[1.] Laboratory of Biological Structure Mechanics (LaBS), Department of Chemistry, Materials and Chemical Engineering "Giulio Natta", Politecnico di Milano, Italy

[2.] PoliTo[BIO]Med Lab, Department of Mechanical and Aerospace Engineering, Politecnico di Torino, Turin, Italy

Address for correspondence:

Francesco Migliavacca

Laboratory of Biological Structure Mechanics

Department of Chemistry, Materials and Chemical Engineering "Giulio Natta"

Politecnico di Milano

Piazza L. da Vinci, 32

20133 Milano, Italy

Phone: +39.02.2399.4316

Fax: +30.02.2399.4286

E-mail: francesco.migliavacca@polimi.it

Accepted chapter available at https://doi.org/10.1016/C2017-0-03308-6

Abstract

The outcome of a stenting procedure is related to a number of factors, among which the hemodynamic perturbations generated by the presence of the stent within the lumen. Computer models are appropriate tools to give insights on this aspect, especially now that knowledge of the specific stent location in an artery can be achieved with advanced intravascular imaging techniques, such as optical coherence tomography. This chapter reviews the main patient-specific studies investigating the local hemodynamics of stented coronary arteries. Particular attention is dedicated to the methodologies developed for the inclusion of the stent geometry in the 3D vessel fluid domain.

Keywords

Stent, coronary artery, intravascular imaging, optical coherence tomography, patient-specific reconstruction, mathematical models, computational fluid dynamics, wall shear stress

1. Introduction

Coronary stents are wire mesh tubular structures that are expanded inside an atherosclerotic coronary artery by balloon expansion to restore the correct blood flow to the heart and to hold the vessel open in the years after the intervention. The main biomechanical effects due to the stent implantation are (i) the damage caused to the arterial wall, which can induce an inflammatory reaction (refer to Chapter 26), (ii) the new local fluid dynamics generated by the protrusion of the stent struts inside the lumen, which can cause an abnormal sensing to the endothelial cells and accumulation of activated platelets due to high or low wall shear stresses (WSSs), and (iii) the drug distribution to the arterial tissue based on the position of the expanded stent struts linked to the fluid dynamic field.

Computer models can elucidate and give insights on some of these aspects. Simplified models based on a 2D geometry have shown that stent struts lead to local flow disturbances with areas of recirculation downstream the struts (Fig. 1) [1–3]. The malapposed stent struts (i.e. struts not in contact with the arterial wall) disrupt the flow and generate regions with high shear rate [2,4,5], which might increase the risk of stent thrombosis [5–7]. Furthermore, the coupling of mass transport and fluid dynamic models, even if in simplified 2D models, brought to the important conclusion that the deposition of the drug in the vessel was more related to the local blood flow alterations than to the drug deposited between the stent struts and the vessel [1]. Again, the location of apposed or malapposed struts has implication on the fluid dynamics and, consequently, also on the drug deposition.

<Figure 1 near here>

Although 2D models can give general indications on the main effects of a stent implantation, knowledge of the specific behaviour of the stent in an artery can be achieved only with detailed 3D models. Indeed, when considering a coronary artery, the main hemodynamic effect of a stent is an

overall reduction of the WSS in the entire treated region in the immediate post-implantation period. As an example, Figure 2 shows the comparison between the time-averaged WSS distribution along the lumen of the same patient-specific coronary artery model with and without the stent presence. In this comparison, the boundary conditions and all the settings of the computational fluid dynamics (CFD) simulations were kept constant [8]. The stented scenario exhibited a significantly lower mean time-averaged WSS as compared to the scenario without stent (0.599 Pa vs. 1.020 Pa). Furthermore, the stented scenario was characterized by a larger percent lumen area exposed to very low time-averaged WSS (i.e. < 0.4 Pa) as compared to the other case (35.0 % versus 2.6 %). For additional details about these CFD simulations, the reader is referred to [8].

The present Chapter reviews the main patient-specific studies investigating the local hemodynamics of post-operative coronary arteries with particular emphasis on the methodologies developed for the inclusion of the stent geometry in the 3D vessel fluid domain.

<Figure 2 near here>

2. Patient-specific CFD simulations of stented coronary arteries

Patient-specific CFD analyses of stented coronary arteries are usually performed to investigate the relation between the hemodynamic perturbations provoked by the stent struts and adverse events, such as in-stent restenosis, or to compare different stents or stenting techniques in subject-specific anatomies from the hemodynamic viewpoint (‘patient-specific virtual bench testing’) [9,10]. The construction of 3D patient-specific stented coronary artery geometries for CFD analysis requires to process clinical images. Different imaging modalities for coronary arteries can be used for 3D reconstruction, including conventional angiography, computed tomography (CT) angiography, intravascular ultrasound (IVUS), and intravascular optical coherence tomography (OCT). To reconstruct the vessel geometry, state-of-the-art methodologies rely on the combination of intravascular imaging techniques, which enable an accurate detection of lumen contours, with two

angiography projections or CT images, which provide a reference in the 3D space [11]. However, the inclusion of the stent geometry in the vessel lumen model still represents a challenge. Until now, the following three main strategies have been proposed to obtain a stented coronary artery fluid domain:

- Drawing of the stent geometry within the patient-specific vessel using a computer-aided design (CAD) software ('CAD drawing');
- Finite element (FE) analyses of stent deployment replicating the real stenting procedure followed to treat the patient ('Stent deployment FE analysis');
- Reconstruction of the stent from OCT images ('from OCT').

Table 1 summarizes the recent patient-specific CFD studies on stented coronary arteries by specifying the strategy adopted for stent reconstruction. The description of the three reconstruction strategies follow, together with the main results obtained in those studies.

2.1 Stent drawing by computer-aided design software

Gundert et al. [12] and Ellwein et al. [13] proposed a method for including the stent in the post-operative coronary artery geometry based on CAD software use. The method consists of the following three main steps: (i) 3D reconstruction of the post-operative lumen model from clinical images; (ii) creation of an idealized model of a thick stent matching the coronary artery geometry; (iii) generation of the fluid domain by subtracting the stent volume from the coronary lumen model. Figure 3 illustrates an example of generation of a stented fluid domain from OCT data. The method requires few hours for the creation of a stented geometry without the need for numerical computation of the expanded stent configuration [12]. However, it does not allow replicating the exact real location of the stent struts inside the coronary artery, being unable to model the non-uniform expansion of stent cells.

<Figure 3 near here>

In Gundert et al. [12], the lumen model of a patient-specific left anterior descending coronary artery (LAD) with one bifurcation was reconstructed from CT images. The study aimed at comparing the local hemodynamics of two different stent designs (i.e. an open-cell ring-and-link and a closed-cell slotted tube prototype stent). Although in both cases regions with low time-averaged WSS were present next to the stent struts and were more prevalent distal to the bifurcation, the case with the open-cell stent resulted in a larger lumen area exposed to low time-averaged WSS.

In Ellwein et al. [13], a patient-specific left circumflex artery (LCx) was reconstructed from OCT. The model of the Cypher stent (Cordis Corp., USA), which was the device implanted in that patient, was included in the post-operative fluid domain using the previously described method. A 6-month follow-up model was also created from OCT. The CFD simulations showed that the post-stenting model was characterized by a higher percent lumen area exposed to low time-averaged WSS than the follow-up model, highlighting that the regions exposed to low WSS returned to physiological levels at follow-up. Additionally, a preliminary relation between the regions with low WSS of the post-stenting model and the highest neointimal regrowth measured at the corresponding follow-up OCT cross-sections was found.

2.2 Finite element analysis of stent deployment

In several studies, patient-specific finite element (FE) analyses of stent deployment were performed to obtain the post-operative anatomy for hemodynamic investigation. Figure 4 shows the general workflow of this method, which is characterized by (i) the creation of the of the pre-operative coronary artery geometry from clinical images, (ii) the virtual stenting simulation replicating all the clinical procedural steps, and (iii) the extraction of the stented fluid domain from the final geometrical configuration obtained with the FE analysis. Detailed information about stent deployment structural simulations in coronary bifurcations are reported in Chapter 26.

<Figure 4 near here>

In 2013, Chiastra et al. [8] demonstrated the feasibility of investigating the local hemodynamics of patient-specific stented coronary bifurcation models obtained after structural simulation. Two pathologic LAD with their bifurcations were reconstructed from conventional angiography and CT. A Xience Prime (Abbott Vascular, USA) and two Endeavor Resolute (Medtronic, USA) stents were virtually implanted in the two pre-operative anatomies, respectively, as previously described [14]. The CFD results highlighted that regions with low WSS were present close to the stent struts, in the region of the bifurcations and, in the case with two stents, in the overlapping zone between the devices. In addition to the near-wall hemodynamics (e.g. calculation of WSS and WSS-based descriptors), the bulk flow was investigated by analyzing the helicity, which describes the arrangement of fluid streams into spiral patterns as they evolve within vessels [15] and has been suggested to have an atheroprotective role in the coronary tree [16]. The study showed that the helical flow patterns originated mainly in the region proximal to the stent as a consequence of the vessel shape and in the bifurcations, and gradually disappeared in the stented region because of the vessel straightening provoked by the device. Furthermore, smaller helical structures were found generated by the stent struts protruding into the lumen. Their role on restenosis, either beneficial or detrimental, was not clarified and further investigation is still needed.

Two more recent studies [17,18] showed the use of sequential stent deployment FE analysis and CFD simulation to compare different stenting techniques and stent platforms in patient-specific vessel geometries, as a potential tool for in silico clinical trials and pre-operative planning. In particular, Mortier et al. [17] investigated the local hemodynamics in a patient-specific left main coronary bifurcation reconstructed from angiography and IVUS. CFD simulations were used to compare the stent sizing strategy performed in vivo with respect to an alternative one (i.e. implantation of 3.0 mm vs. 3.5 mm Abbott Xience Prime stent). Chiastra et al. [18] investigated the hemodynamics of two patient-specific anatomies (i.e. a LAD and a LCx with bifurcations) reconstructed from CT and OCT.

Specifically, the authors analyzed the impact on the WSS distribution of the implantation of different stent platforms and positions.

Although computationally expensive, this method allows the comparison of patient-specific stented models in terms of different types of biomechanical quantities. In fact, in addition to hemodynamic quantities, geometrical (e.g. stent malapposition) and mechanical quantities (e.g. stress and strain within the arterial vessel) can be computed, resulting in a more comprehensive biomechanical analysis.

2.3 Stent reconstruction from optical coherence tomography data

Currently, OCT is the best imaging technique that allows the accurate detection of both lumen contours and stent struts because of its superior in-plane resolution (i.e. axial resolution of 12-15 μm and lateral resolution of 20-40 μm [19]) as compared to the other imaging modalities available for coronary arteries [20]. This feature enables the direct 3D reconstruction of post-operative coronary artery models that include the actual stent geometry without the execution of stent deployment FE analysis. Until now, many (semi)-automatic segmentation algorithms have been proposed, as extensively reviewed in [20]. Furthermore, different methods have been developed for the creation of 3D stented vessel models suitable for CFD analysis starting from the segmented OCT images [20,21].

In a number of studies [22–27], the patient-specific stented models were reconstructed following these steps: (i) detection of the lumen contours accounting for the stent (or bioresorbable scaffold) struts in each OCT frame; (ii) placement of the segmented contours perpendicular to the vessel centerline extracted from two angiographic projections; (iii) estimation of proper orientation of the OCT frames by using the side branches visible in both OCT and angiographic images as landmarks; (iv) connection of the segmented contours by generating a non-uniform rational B-spline surface that represents the stented vessel.

As regards the hemodynamic investigation performed in those studies, a few of them [22–24] focused on the relation between WSS and neointimal thickness in patients treated with the Absorb Bioresorbable Vascular Scaffold (BVS) (Abbott Vascular, USA). An inverse correlation was found between baseline WSS and neointimal thickness at 6-month or 1-year follow-up. While the analysis of Papaflakis et al. [22] was limited to one patient-specific case, Bourantas et al. [23] found a statistically significant inverse correlation between the logarithmic transformed baseline WSS and neointimal thickness at 1-year follow-up in 12 patients (average $r=-0.451$; $p < 0.001$). It is worth noting that in this study only OCT data were used to reconstruct the stented vessel models with the result that their real 3D shape was not reproduced. Conversely, in another work by the same research group [24], OCT and angiography images were combined to reconstruct 6 patient-specific stented vessels. An inverse correlation was also observed between the logarithmic transformed baseline WSS and neointimal thickness at 1-year follow-up ($r=-0.52 \pm 0.19$, $p=0.028$). Recent studies [25–27] compared the WSS distribution immediately after stent implantation with that at 5-year follow-up in patients treated with the Absorb BVS. In particular, Thondapu et al. 2018 [27] showed that the WSS was higher at follow-up in 7 patient-specific cases. More in detail, the percent lumen area exposed to low time-averaged WSS (< 1 Pa) significantly decreased over 5 years (15.92% vs. 4.99%, $p < 0.0001$), while moderate (1–7 Pa) and high WSS (> 7 Pa) did not significantly change (moderate WSS: 76.93% vs. 80.7%, $p = 0.546$; high ESS: 7.15% vs. 14.31%, $p = 0.281$). Furthermore, a positive correlation was found ($p < 0.0001$) between baseline ESS and change in lumen area at 5-years follow-up.

Differently from the previously mentioned works, Gogas et al. [28,29] performed a preliminary local hemodynamic analysis of two patient-specific cases treated with the Absorb BVS that were reconstructed using an alternative method, based on the combination of OCT and angiographic images and an interactive scaffold pattern interpretation algorithm. This reconstruction method comprises the following steps: (i) classification of the scaffold strut points detected from OCT as belonging to the links or the rings of the device by using an in-house developed pattern interpretation

algorithm; (ii) positioning of the scaffold strut points of each ring/link along the arterial centerline obtained from two angiographic projections; (iii) interpolation of the scaffold strut points using cubic splines to construct a continuous 3D scaffold skeleton; (iv) creation of the final scaffold model by automatically placing and connecting rectangular cross-sections along the skeleton lines.

Li et al. [30] investigated the WSS patterns in 10 patient-specific coronary bifurcations treated with the DESolve bioresorbable scaffold (Elixir Medical, USA). The stented geometries were obtained by fusing OCT images with two angiographic projections. An in-house developed surface reconstruction algorithm based on an adapted marching cube algorithm was used to reconstruct the 3D patient-specific bioresorbable scaffold geometry starting from semi-automatically delineated strut contours. CFD analyses were performed in the same lumen models with and without the presence of the bioresorbable scaffold. The inclusion of the bioresorbable scaffold geometry resulted in lower time-averaged WSS at the inter-strut zones and larger degree of shear oscillation and spatial WSS heterogeneity, in particular at the side branch ostia. Additionally, the effect of the stent strut thickness on WSS was analyzed by considering bioresorbable scaffold models with reduced strut thickness (i.e. 100 μm instead of 150 μm). The cases with thinner struts resulted in less WSS heterogeneity.

Finally, in Migliori et al. [31], one patient-specific stented model of a coronary bifurcation treated with the Absorb BVS was obtained using a 3D reconstruction method based on prior stent design knowledge. This procedure was previously validated on a stented bifurcated coronary artery phantom [24,25]. Specifically, the construction of the patient-specific 3D stent model consisted of the following steps (Fig. 5): (i) creation of the stent skeleton in its straight, free-expanded configuration; (ii) morphing of the skeleton lines on points that belong to the stent point cloud obtained from OCT so that their distance was minimized; (iii) generation of the 3D patient-specific stent model by connecting cross-section curves placed along the stent skeleton lines. A similar stent reconstruction method was also developed by a different research group, but it was exclusively applied to animal OCT data [32].

Since WSS calculation is highly dependent on the local geometry of the stented coronary artery, the reconstruction of an accurate patient-specific stent geometry is fundamental to obtain reliable CFD results [20]. A comparison between the different techniques for obtaining the stented vessel geometry has not been performed yet. In contrast to other strategies [22–27], the method based on prior stent design knowledge enables the generation of models that present continuous stent geometry and the real stent strut cross-sectional shape, and hence it appears as the most promising and accurate. However, this reconstruction method is time-consuming and requires extensive user intervention during the stent skeleton morphing phase. Recently, preliminary strategies for automating the registration between the stent skeleton and the OCT stent point cloud have been proposed [33,34]. Nevertheless, further advancements are still required for automating the stent skeleton morphing step in case of patient-specific cases.

<Figure 5 near here>

3. Boundary conditions for patient-specific CFD analyses

In addition to the 3D reconstruction of (stented) coronary artery geometry from clinical images, subject-specific boundary conditions are required to perform proper patient-specific CFD analyses.

As regards the inlet boundary condition, the patient-specific inlet flow-rate can be estimated from angiography using the frame count method, as performed in several studies summarized in Table 1 [22,24,26,30,31]. This method consists in counting the number of cine-angiographic frames for the contrast agent to pass from the inlet to the outlet of a vessel section free of significant side branches. The following similar formulas can be applied to compute the volume flow-rate (Q) depending on whether the volume of the vessel [35] or the length of its centerline [36] is estimated:

$$Q = \frac{f \cdot V}{\#frames} \quad (1)$$

$$Q = \frac{f \cdot l \cdot A}{\#frames} \quad (2)$$

where *f* is the cine-angiography frame-rate, *#frames* the number of counted frames, *V* the volume and *l* the length of the vessel section under consideration, and *A* the vessel inlet cross-sectional area.

Alternatively, dual-sensor pressure and Doppler velocity wires might be used to measure the velocity in vivo at multiple locations of the coronary branches. The measured velocity waveforms and the derived flow-rates might be applied as boundary condition of the patient-specific CFD model. However, these measurements are rarely carried out in the clinical routine because of their high invasiveness.

As regards the outlet boundary conditions, in the absence of in vivo measurements, the flow distributions among the coronary branches (if modeled) can be estimated using diameter-based scaling laws [37]. Given a coronary bifurcation with daughter branches characterized by diameters D_1 and D_2 and flow-rates Q_1 and Q_2, the following scaling laws are commonly used:

- Murray's law [38], which relies on the principle of minimum energy

$$\frac{Q_{D2}}{Q_{D1}} = \left(\frac{Q_{D2}}{Q_{D1}}\right)^3 \tag{3}$$

- HK model [39], which is based on the assumption of a fractal-like branching pattern in a tree structure

$$\frac{Q_{D2}}{Q_{D1}} = \left(\frac{Q_{D2}}{Q_{D1}}\right)^{\frac{7}{3}} \tag{4}$$

- van der Giessen's law [40], which was obtained by fitting the flow-rate and diameter measurements in human coronary arteries provided by Doriot et al. [41]

$$\frac{Q_{D2}}{Q_{D1}} = \left(\frac{Q_{D2}}{Q_{D1}}\right)^{2.27} \tag{5}$$

van der Giessen's law was used in some studies of Table 1 [8,17,31]. As an alternative to the diameter-based scaling laws, the 3D model of the stented vessel can be coupled with a lumped parameter model (i.e. 0D model) made of resistances, compliances, and inductances, which represent the downstream coronary vasculature. This modeling strategy was adopted in other

studies reported in Table 1 [12,13,18]. The critical aspect of this strategy is the estimation of the parameters in case of lack of in vivo pressure and velocity measurements.

4. Blood model

In the patient-specific CFD studies summarized in Table 1, blood was modeled as an incompressible, homogeneous fluid with constant density and viscosity described using a Newtonian [12,13,18,22–24,26,30] or non-Newtonian model [8,17,25,27,31]. In several studies [8,17,31], the Carreau model was chosen as non-Newtonian model to take into account the shear thinning properties of blood. In this model, the viscosity is written as:

$$\mu = \mu_\infty + (\mu_0 - \mu_\infty) \cdot \left[1 + \left(\lambda \dot{S}\right)^2\right]^{(n-1)/2} \quad (6)$$

where μ is the dynamic viscosity, μ_0 and μ_∞ are the viscosity values as the shear rate goes to zero and infinity respectively, $\dot{S}$ is the shear rate, λ is the time constant, and n is the Power-Law index. In two studies [25,27], the non-Newtonian behavior of blood was described using Quemada's model [42,43], in which viscosity changes depending on shear rate and haematocrit as follows:

$$\mu = \frac{\mu_P}{\left(1-\frac{1}{2}kH\right)^2} \quad (7)$$

where μ_P is the viscosity of the suspending fluid, H is the concentration of suspended particles (i.e. heamatocrit), and k is an intrinsic viscosity calculated as:

$$k = \frac{k_0 + k_\infty \sqrt{\dot{S}/S_C}}{1+\sqrt{\dot{S}/S_C}} \quad (8)$$

where k_0, k_∞, *and* S_C are three parameters that are functions of particle concentration H.

The selection of one non-Newtonian model for blood viscosity rather than another has a degree of arbitrariness. Previous investigations showed that the blood shear thinning behavior seems to be the dominant non-Newtonian property [44]. Therefore, non-Newtonian models considering the shear thinning behavior of blood in similar ways should generate comparable results. Moreover, the

necessity of including the non-Newtonian blood behavior for studying the hemodynamics in coronary arteries is still subject of debate. Johnston et al. [45] showed that the effect of a non-Newtonian blood model was only significant for a portion (i.e. approximately 30%) of the cardiac cycle of transient CFD simulations of imaged-based right coronary arteries. Thus, the researchers concluded that the choice of the Newtonian model for blood viscosity might be an acceptable approximation for the WSS calculation. Recently, Arzani [46] proposed a novel non-Newtonian model in which the blood shear thinning behavior is activated in high residence-time regions. In contrast to current non-Newtonian models, Arzani's model account for the rouleaux formation, which plays a major role in blood shear-thinning behavior. The study showed that the activation of shear-thinning behavior only in regions of high flow stagnation resulted in WSS patterns qualitatively similar and quantitatively closer to the Newtonian model as compared to a conventional non-Newtonian model (i.e. Carreau-Yasuda model). Further investigation is required as in Arzani's study the novel viscosity model was applied only to an internal carotid artery aneurysm and an abdominal aortic aneurysm imaged-based cases, without analyzing any coronary artery case.

5. CFD model validation

The number of studies reporting a validation of the CFD models of complex stented vessel geometries with respect to in vitro experiments is rather limited. Raben et al. [47] compared the steady-state velocity field measured in several stented and non-stented bifurcations phantoms (with three bifurcation angles and four different single- and double-stenting techniques) by means of digital particle image velocimetry (PIV) with corresponding CFD results. In general, a good qualitative agreement between experimental and numerical results was found. Both techniques were able to identify regions of low and recirculating flow. García García et al. [48] obtained good agreement in terms of velocity field between experimental PIV data and CFD results in four stented bifurcated coronary phantoms in both steady-state and pulsatile conditions. The hemodynamics of

four bifurcated coronary phantoms with one or two implemented stents was analyzed. To reduce the geometrical uncertainties in the replicated computational models, the stented bifurcated phantoms were scanned after stent deployment using micro-computed tomography. In addition, the same research group [49] provided a series of controlled and detailed velocity PIV measurements obtained in a simplified coronary bifurcation phantom with different stent configurations, for use as a benchmark for CFD model validation.

In the previous mentioned studies, the CFD results in terms of WSS distribution along the vessel lumen were not validated. The calculation of WSS requires the precise knowledge of the three-directional velocity field next to the vessel lumen. Studies that use a 3D PIV system for WSS calculation have not been proposed yet because of the technical complexity of measuring the velocity field in the proximity of the walls of a stented silicone phantom with the dimension of a coronary artery. Brindise et al. [50] estimated the WSS in four stented bifurcation phantoms from experimental PIV data and investigated the impact of three stenting implantation techniques against one unstented scenario. However, their analysis was limited to the plane of the bifurcations as a standard 2D PIV system was used. Furthermore, a comparison against numerical results was not performed.

In vivo validation of velocity patterns and WSS in stented coronary arteries is still unfeasible with current imaging techniques. In fact, currently, blood flow 3D velocity data can be acquired in vivo only using 4D flow magnetic resonance imaging, whose spatial resolution is sufficient for 3D velocity field and WSS measurements in large vessels (e.g. in the aorta [51]), but not in smaller vessels as coronary arteries with stents.

6. Conclusions and future directions

This Chapter provided a review of the hemodynamics generated by the stent implantation in in silico, patient-specific models. Good progresses have been made in the recent years. Until now, different techniques have been proposed to obtain the 3D stented coronary artery models for CFD

analysis. Investigation on the impact of these techniques as well as of specific geometric parameters (e.g. OCT interslice distance for the lumen reconstruction) on the hemodynamic results is missing and would be very useful to quantitatively identify the most accurate reconstruction strategy. The future of these CFD models - maybe not too far - is their usage in clinical routine to get additional information for the clinicians in terms of hemodynamic indexes when implanting a stent. For this purpose, significant improvements are still needed in terms of automation of the 3D stented vessel reconstruction method from OCT images and reduction of the computational costs of the CFD simulations.

7. Acknowledgments

None

8. References

[1] Balakrishnan B, Tzafriri AR, Seifert P, Groothuis A, Rogers C, Edelman BR. Strut position, blood flow, and drug deposition: Implications for single and overlapping drug-eluting stents. Circulation 2005;111:2958–65. doi:10.1161/CIRCULATIONAHA.104.512475.

[2] Foin N, Torii R, Mattesini A, Wong P, Di Mario C. Biodegradable vascular scaffold: is optimal expansion the key to minimising flow disturbances and risk of adverse events? EuroIntervention 2015;10:1139–42. doi:10.4244/EIJY14M11_09.

[3] Foin N, Lee RD, Torii R, Guitierrez-Chico JL, Mattesini A, Nijjer S, et al. Impact of stent strut design in metallic stents and biodegradable scaffolds. Int J Cardiol 2014;177:800–8. doi:10.1016/j.ijcard.2014.09.143.

[4] Foin N, Gutiérrez-Chico JL, Nakatani S, Torii R, Bourantas C V., Sen S, et al. Incomplete stent apposition causes high shear flow disturbances and delay in neointimal coverage as a function of strut to wall detachment distance implications for the management of incomplete

stent apposition. Circ Cardiovasc Interv 2014;7:180–9. doi:10.1161/CIRCINTERVENTIONS.113.000931.

[5] Kolandaivelu K, Swaminathan R, Gibson WJ, Kolachalama VB, Nguyen-Ehrenreich KL, Giddings VL, et al. Stent thrombogenicity early in high-risk interventional settings is driven by stent design and deployment and protected by polymer-drug coatings. Circulation 2011;123:1400–9. doi:10.1161/CIRCULATIONAHA.110.003210.

[6] Ng J, Bourantas C V., Torii R, Ang HY, Tenekecioglu E, Serruys PW, et al. Local hemodynamic forces after stenting: implications on restenosis and thrombosis. Arterioscler Thromb Vasc Biol 2017;In press. doi:10.1161/ATVBAHA.117.309728.

[7] Foin N, Lu S, Ng J, Bulluck H, Hausenloy D, Wong P, et al. Stent malapposition and the risk of stent thrombosis: mechanistic insights from an in vitro model. EuroIntervention 2017;13:e1096–8. doi:10.4244/EIJ-D-17-00381.

[8] Chiastra C, Morlacchi S, Gallo D, Morbiducci U, Cárdenes R, Larrabide I, et al. Computational fluid dynamic simulations of image-based stented coronary bifurcation models. J R Soc Interface 2013;10:20130193. doi:10.1098/rsif.2013.0193.

[9] Antoniadis AP, Mortier P, Kassab G, Dubini G, Foin N, Murasato Y, et al. Biomechanical Modeling to Improve Coronary Artery Bifurcation Stenting: Expert Review Document on Techniques and Clinical Implementation. JACC Cardiovasc Interv 2015;8:1281–96. doi:10.1016/j.jcin.2015.06.015.

[10] Migliavacca F, Chiastra C, Chatzizisis YS, Dubini G. Virtual bench testing to study coronary bifurcation stenting. EuroIntervention 2015;11 Suppl V:V31–4. doi:10.4244/EIJV11SVA7.

[11] Papafaklis MI, Bourantas C V, Yonetsu T, Vergallo R, Kotsia A, Nakatani S, et al. Anatomically correct three-dimensional coronary artery reconstruction using frequency domain optical coherence tomographic and angiographic data: head-to-head comparison with intravascular ultrasound for endothelial shear stress assessment in humans. EuroIntervention 2015;11:407–15. doi:10.4244/EIJY14M06_11.

[12] Gundert TJ, Shadden SC, Williams AR, Koo BK, Feinstein J a., Ladisa JF. A rapid and computationally inexpensive method to virtually implant current and next-generation stents into subject-specific computational fluid dynamics models. Ann Biomed Eng 2011;39:1423–37. doi:10.1007/s10439-010-0238-5.

[13] Ellwein LM, Otake H, Gundert TJ, Koo B-K, Shinke T, Honda Y, et al. Optical Coherence Tomography for Patient-specific 3D Artery Reconstruction and Evaluation of Wall Shear Stress in a Left Circumflex Coronary Artery. Cardiovasc Eng Technol 2011;2:212–27. doi:10.1007/s13239-011-0047-5.

[14] Morlacchi S, Colleoni SG, Cárdenes R, Chiastra C, Diez JL, Larrabide I, et al. Patient-specific simulations of stenting procedures in coronary bifurcations: two clinical cases. Med Eng Phys 2013;35:1272–81. doi:10.1016/j.medengphy.2013.01.007.

[15] Morbiducci U, Ponzini R, Grigioni M, Redaelli A. Helical flow as fluid dynamic signature for atherogenesis risk in aortocoronary bypass. A numeric study. J Biomech 2007;40:519–34. doi:10.1016/j.jbiomech.2006.02.017.

[16] De Nisco G, Kok AM, Chiastra C, Gallo D, Hoogendoorn A, Migliavacca F, et al. The Atheroprotective Nature of Helical Flow in Coronary Arteries. Ann Biomed Eng 2018. doi:10.1007/s10439-018-02169-x.

[17] Mortier P, Wentzel JJ, De Santis G, Chiastra C, Migliavacca F, De Beule M, et al. Patient-specific computer modelling of coronary bifurcation stenting: the John Doe programme. EuroIntervention 2015;11 Suppl V:V35–9. doi:10.4244/EIJV11SVA8.

[18] Chiastra C, Wu W, Dickerhoff B, Aleiou A, Dubini G, Otake H, et al. Computational replication of the patient-specific stenting procedure for coronary artery bifurcations: From OCT and CT imaging to structural and hemodynamics analyses. J Biomech 2016;49:2102–11. doi:10.1016/j.jbiomech.2015.11.024.

[19] Nammas W, Ligthart JMR, Karanasos A, Witberg KT, Regar E. Optical coherence tomography for evaluation of coronary stents in vivo. Expert Rev Cardiovasc Ther

2013;11:577–88. doi:10.1586/erc.13.37.

[20] Chiastra C, Migliori S, Burzotta F, Dubini G, Migliavacca F. Patient-Specific Modeling of Stented Coronary Arteries Reconstructed from Optical Coherence Tomography: Towards a Widespread Clinical Use of Fluid Dynamics Analyses. J Cardiovasc Transl Res 2018;11:156–72. doi:10.1007/s12265-017-9777-6.

[21] Tenekecioglu E, Albuquerque FN, Sotomi Y, Zeng Y, Suwannasom P, Tateishi H, et al. Intracoronary optical coherence tomography: Clinical and research applications and intravascular imaging software overview. Catheter Cardiovasc Interv 2017;89:679–89. doi:10.1002/ccd.26920.

[22] Papafaklis MI, Bourantas C V., Farooq V, Diletti R, Muramatsu T, Zhang Y, et al. In vivo assessment of the three-dimensional haemodynamic micro-environment following drug-eluting bioresorbable vascular scaffold implantation in a human coronary artery: Fusion of frequency domain optical coherence tomography and angiography. EuroIntervention 2013;9:890. doi:10.4244/EIJV9I7A147.

[23] Bourantas C V., Papafaklis MI, Kotsia A, Farooq V, Muramatsu T, Gomez-Lara J, et al. Effect of the endothelial shear stress patterns on neointimal proliferation following drug-eluting bioresorbable vascular scaffold implantation: An optical coherence tomography study. JACC Cardiovasc Interv 2014;7:315–24. doi:10.1016/j.jcin.2013.05.034.

[24] Bourantas C V., Papafaklis MI, Lakkas L, Sakellarios A, Onuma Y, Zhang YJ, et al. Fusion of optical coherence tomographic and angiographic data for more accurate evaluation of the endothelial shear stress patterns and neointimal distribution after bioresorbable scaffold implantation: Comparison with intravascular ultrasound-derived rec. Int J Cardiovasc Imaging 2014;30:485–94. doi:10.1007/s10554-014-0374-3.

[25] Thondapu V, Tenekecioglu E, Poon EKW, Onuma Y, Serruys PW. Improvement in local haemodynamics 5 years after implantation of a coronary bioresorbable scaffold: a pulsatile non-Newtonian shear stress analysis. Eur Hear J - Cardiovasc Imaging 2017.

doi:10.1093/ehjci/jex165.

[26] Torii R, Tenekecioglu E, Bourantas C, Poon E, Thondapu V, Gijsen F, et al. Five-year follow-up of underexpanded and overexpanded bioresorbable scaffolds: self-correction and impact on shear stress. EuroIntervention 2017;12:2158–9. doi:10.4244/EIJ-D-17-00081.

[27] Thondapu V, Tenekecioglu E, Poon EKW, Collet C, Torii R, Bourantas C V, et al. Endothelial shear stress 5 years after implantation of a coronary bioresorbable scaffold. Eur Heart J 2018;39:1602–9. doi:10.1093/eurheartj/ehx810.

[28] Gogas BD, King SB, Timmins LH, Passerini T, Piccinelli M, Veneziani A, et al. Biomechanical assessment of fully bioresorbable devices. JACC Cardiovasc Interv 2013;6:760–1. doi:10.1016/j.jcin.2013.04.008.

[29] Gogas BD, Yang B, Piccinelli M, Giddens DP, King SB, Kereiakes DJ, et al. Novel 3-Dimensional Vessel and Scaffold Reconstruction Methodology for the Assessment of Strut-Level Wall Shear Stress After Deployment of Bioresorbable Vascular Scaffolds From the ABSORB III Imaging Substudy. JACC Cardiovasc Interv 2016;9:501–3. doi:10.1016/j.jcin.2016.01.008.

[30] Li Y, Li Z, Holck EN, Xu B, Karanasos A, Fei Z, et al. Local Flow Patterns After Implantation of Bioresorbable Vascular Scaffold in Coronary Bifurcations - Novel Findings by Computational Fluid Dynamics. Circ J 2018;82:1575–83. doi:10.1253/circj.CJ-17-1332.

[31] Migliori S, Rampat R, Bologna M, Montin E, Burzotta F, Hildick-Smith D, et al. A Patient-Specific Study Investigating the Relation between Coronary Hemodynamics and Neo-Intimal Thickening after Bifurcation Stenting with a Polymeric Bioresorbable Scaffold. Appl Sci 2018;8:1510. doi:10.3390/app8091510.

[32] O'Brien CC, Kolandaivelu K, Brown J, Lopes AC, Kunio M, Kolachalama VB, et al. Constraining OCT with knowledge of device design enables high accuracy hemodynamic assessment of endovascular implants. PLoS One 2016;11:1–18.

doi:10.1371/journal.pone.0149178.

[33] Lin CY, Veneziani A, Ruthotto L. Numerical methods for polyline-to-point-cloud registration with applications to patient-specific stent reconstruction. Int j Numer Method Biomed Eng 2018;34:e2934. doi:10.1002/cnm.2934.

[34] Elliott MR, Kim D, Molony DS, Morris L, Samady H, Joshi S, et al. Establishment of an Automated Algorithm Utilizing Optical Coherence Tomography and Micro-Computed Tomography Imaging to Reconstruct the 3D Deformed Stent Geometry. IEEE Trans Med Imaging 2018:in press. doi:10.1109/TMI.2018.2870714.

[35] Sakamoto S, Takahashi S, Coskun AU, Papafaklis MI, Takahashi A, Saito S, et al. Relation of Distribution of Coronary Blood Flow Volume to Coronary Artery Dominance. Am J Cardiol 2013;111:1420–4. doi:10.1016/j.amjcard.2013.01.290.

[36] Kumar A, Thompson EW, Lefieux A, Molony DS, Davis EL, Chand N, et al. High Coronary Shear Stress in Patients With Coronary Artery Disease Predicts Myocardial Infarction. J Am Coll Cardiol 2018;72:1926–35. doi:10.1016/j.jacc.2018.07.075.

[37] Huo Y, Kassab GS. Scaling laws of coronary circulation in health and disease. J Biomech 2016;49:2531–9. doi:10.1016/j.jbiomech.2016.01.044.

[38] Murray CD. The Physiological Principle of Minimum Work Applied to the Angle of Branching of Arteries. J Gen Physiol 1926;9:835–41.

[39] Huo Y, Kassab GS. Intraspecific scaling laws of vascular trees. J R Soc Interface 2012;9:190–200. doi:10.1098/rsif.2011.0270.

[40] van der Giessen AG, Groen HC, Doriot PA, de Feyter PJ, van der Steen AFW, van de Vosse FN, et al. The influence of boundary conditions on wall shear stress distribution in patients specific coronary trees. J Biomech 2011;44:1089–95. doi:10.1016/j.jbiomech.2011.01.036.

[41] Doriot P a, Dorsaz P a, Dorsaz L, De Benedetti E, Chatelain P, Delafontaine P. In-vivo measurements of wall shear stress in human coronary arteries. Coron Artery Dis 2000;11:495–502. doi:10.1097/00019501-200009000-00008.

[42] Quemada D. Rheology of concentrated disperse systems II. A model for non-newtonian shear viscosity in steady flows. Rheol Acta 1978;17:632–42. doi:10.1007/BF01522036.

[43] Quemada D. Rheology of concentrated disperse systems III. General features of the proposed non-newtonian model. Comparison with experimental data. Rheol Acta 1978;17:643–53. doi:10.1007/BF01522037.

[44] Gijsen FJ, Allanic E, van de Vosse FN, Janssen JD. The influence of the non-Newtonian properties of blood on the flow in large arteries: unsteady flow in a 90 degrees curved tube. J Biomech 1999;32:705–13.

[45] Johnston BM, Johnston PR, Corney S, Kilpatrick D. Non-Newtonian blood flow in human right coronary arteries: Transient simulations. J Biomech 2006;39:1116–28. doi:10.1016/j.jbiomech.2005.01.034.

[46] Arzani A. Accounting for residence-time in blood rheology models: do we really need non-Newtonian blood flow modelling in large arteries? J R Soc Interface 2018;15:20180486. doi:10.1098/rsif.2018.0486.

[47] Raben JS, Morlacchi S, Burzotta F, Migliavacca F, Vlachos PP. Local blood flow patterns in stented coronary bifurcations: an experimental and numerical study. J Appl Biomater Funct Mater 2014;0:0–0. doi:10.5301/jabfm.5000217.

[48] García García J, García Carrascal P, Castro Ruiz F, Manuel Martín F, Fernández JA. Effects of bifurcation-specific and conventional stents on coronary bifurcation flow. An experimental and numerical study. J Biomech 2017;54:64–72. doi:10.1016/j.jbiomech.2017.01.043.

[49] García Carrascal P, García García J, Sierra Pallares J, Castro Ruiz F, Manuel Martín FJ. Benchmark for Numerical Models of Stented Coronary Bifurcation Flow. J Biomech Eng 2018;140:091009. doi:10.1115/1.4039676.

[50] Brindise MC, Chiastra C, Burzotta F, Migliavacca F, Vlachos PP. Hemodynamics of Stent Implantation Procedures in Coronary Bifurcations: An In Vitro Study. Ann Biomed Eng

2016. doi:10.1007/s10439-016-1699-y.

[51] Rodríguez-Palomares JF, Dux-Santoy L, Guala A, Kale R, Maldonado G, Teixidó-Turà G, et al. Aortic flow patterns and wall shear stress maps by 4D-flow cardiovascular magnetic resonance in the assessment of aortic dilatation in bicuspid aortic valve disease. J Cardiovasc Magn Reson 2018;20:28. doi:10.1186/s12968-018-0451-1.

[52] Migliori S, Chiastra C, Bologna M, Montin E, Dubini G, Aurigemma C, et al. A framework for computational fluid dynamic analyses of patient-specific stented coronary arteries from optical coherence tomography images. Med Eng Phys 2017;47:105–16. doi:10.1016/j.medengphy.2017.06.027.

Table

Table 1. List of published studies on computational fluid dynamics simulations of patient-specific stented coronary artery models.

Figures

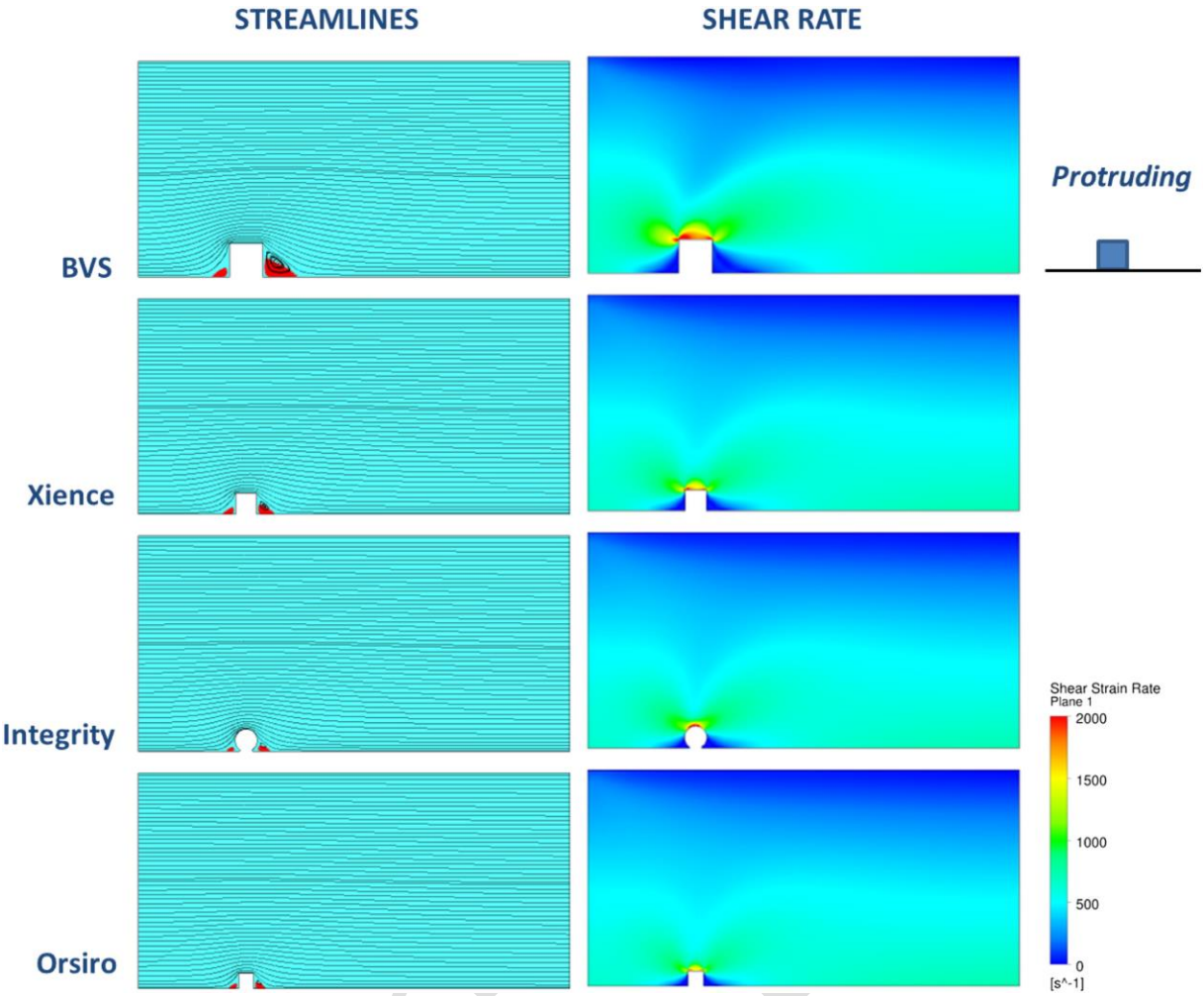

Figure 1. Impact of stent strut design on flow patterns: computed streamlines (left panel) and shear rates (right panel) for 4 different stent strut shapes and strut thickness, namely the Absorb Bioresorbable Vascular Scaffold (BVS) (Abbott Vascular, USA) and the Xience Prime (Abbott Vascular, USA), Resolute Integrity (Medtronic, USA), and Orsiro (Biotronik, Germany) drug eluting stents. Thinner struts create a smaller obstacle for blood flow with lesser shear disturbances. Reprinted with permission from [3].

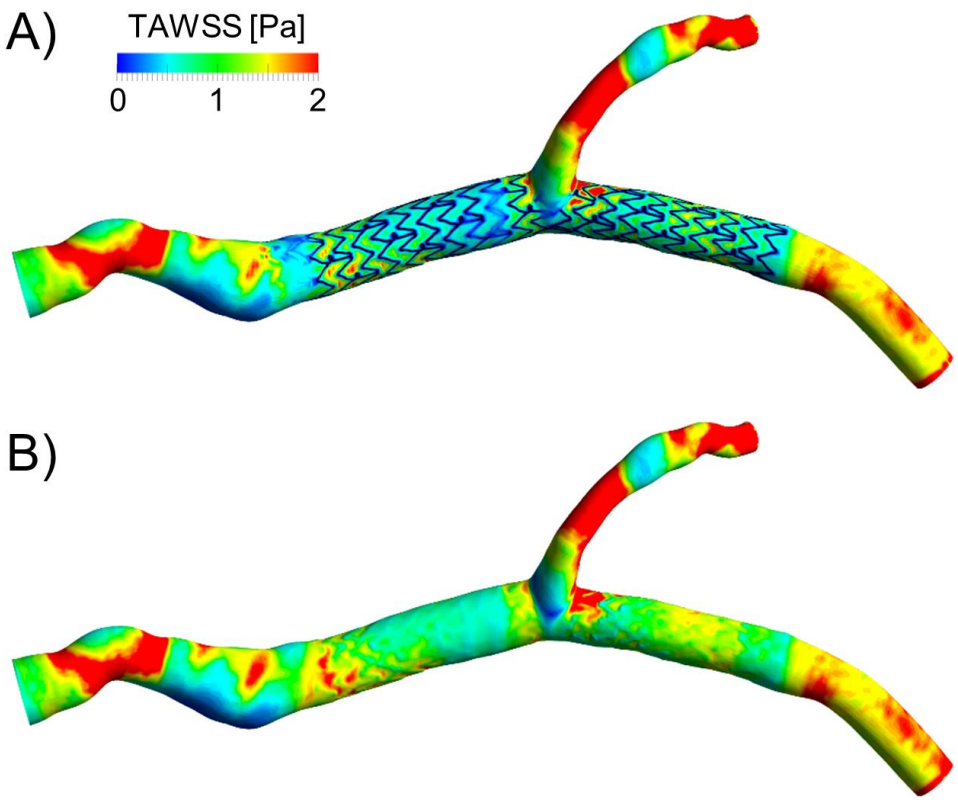

Figure 2. Comparison between the contour map of time-averaged wall shear stress (TAWSS) of a patient-specific coronary artery model with (A) and without (B) the presence of a stent. The coronary artery model represents the proximal portion of the left anterior descending coronary artery and was reconstructed from conventional angiography an computed tomography angiography data [8]. The stent (Xience Prime, Abbott Vascular, USA) was virtually implanted in the coronary artery model by means of finite element analysis replicating all the stent implantation steps performed by the clinicians [8,14]. Figure inspired to [8].

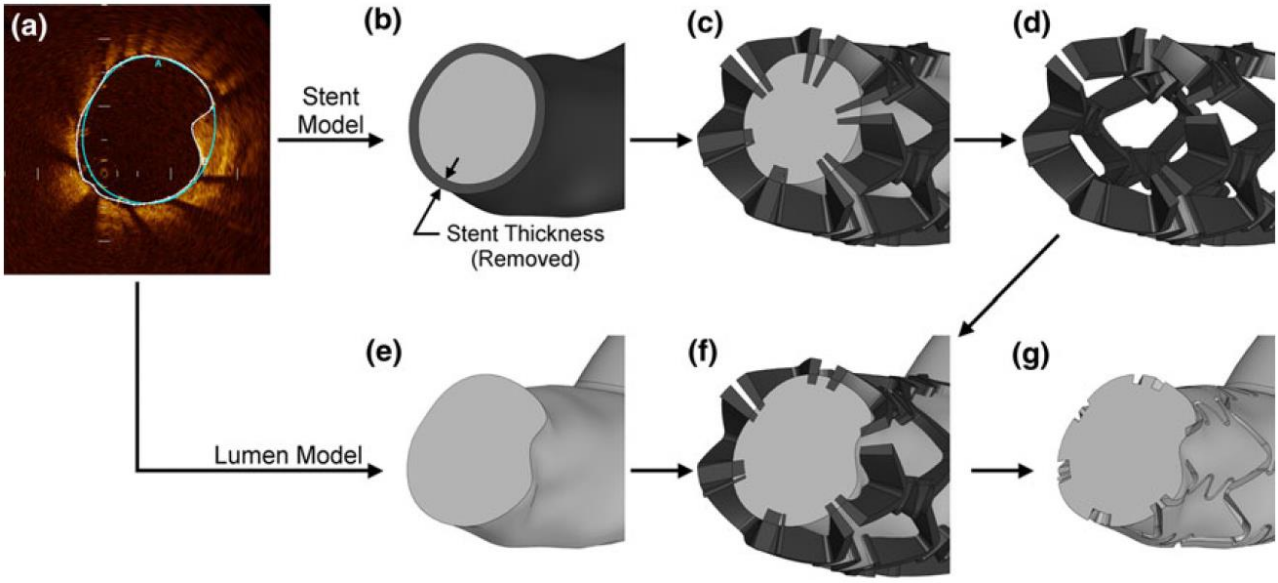

Figure 3. Stent reconstruction method based on computer-aided design drawing of the stent geometry within the patient-specific vessel geometry [12,13]. Solid models of the outer surface of the stent (b) and vessel lumen (e) were lofted from the white and cyan segmentations of the optical coherence tomography images (a). The stent radial thickness was subtracted from the model of lofted stent segmentation (b), which was subsequently subtracted from a thick stent model (c) to create a patient-specific stent model (d). Subtracting the patient-specific stent model (d) from the lumen model (e) as shown in (f) generated a computational representation of the blood flow domain. Reprinted with permission from [13].

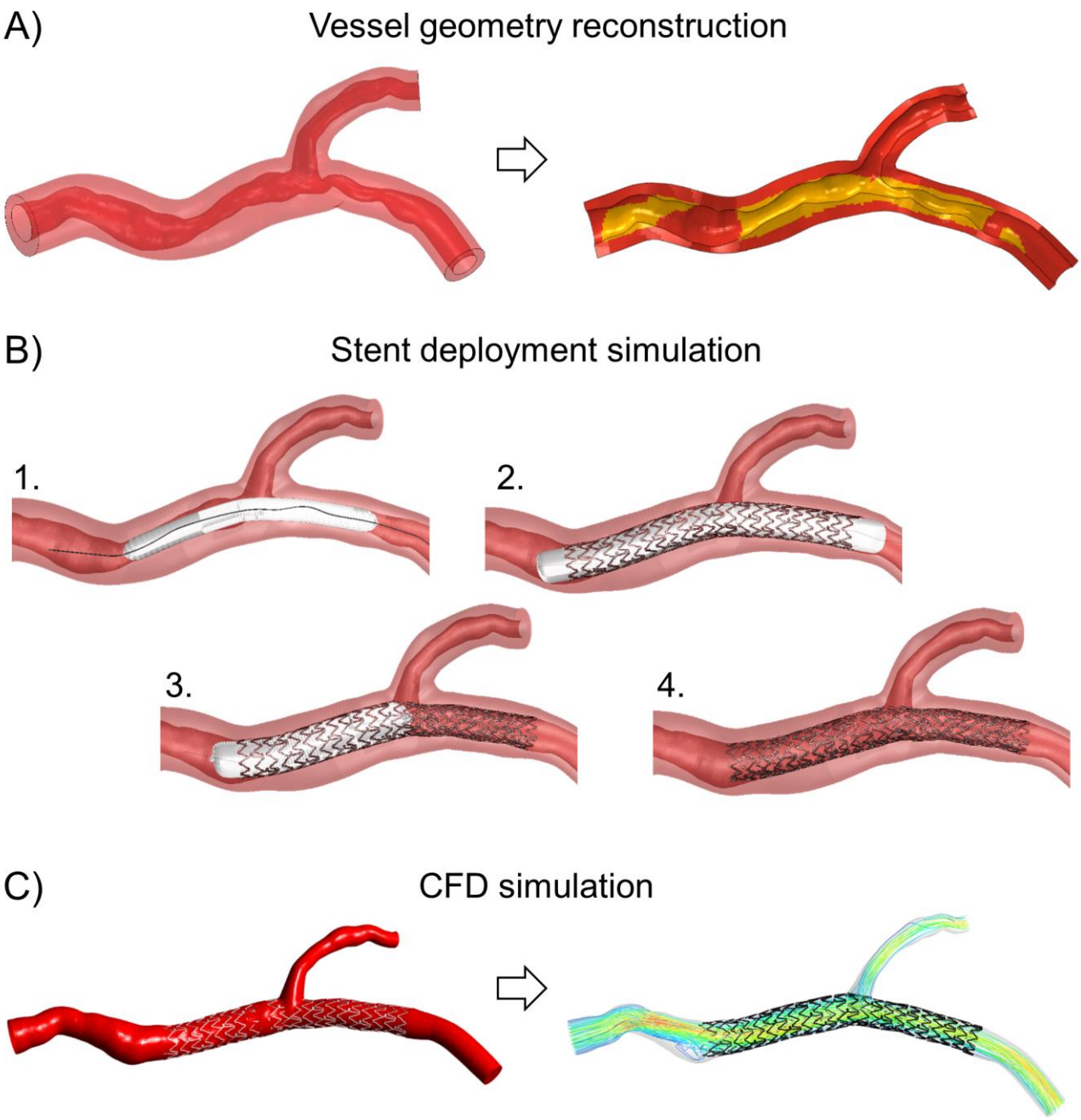

Figure 4. Workflow for computational fluid dynamics investigation of patient-specific stented coronary artery models obtained by virtually deploy the stent using finite element (FE) analysis. The workflow is applied to the diseased proximal portion of a patient-specific left anterior descending coronary artery model [8,14]. A) 3D reconstruction of the coronary vessel from clinical images (left) and identification of the plaque regions (right, highlighted in yellow). B) FE analysis of stent deployment replicating the stenting procedure followed by interventional cardiologists to treat the patient (1- Angioplasty procedure, 2- Deployment of a 3x32 mm Xience Prime stent

(Abbott Vascular, USA), 3- proximal optimization technique using a 3.5x20 mm balloon, and 4- final geometry after stent recoil). C) Extraction of the fluid domain from the final geometry obtained from the structural analysis (left) and execution of the CFD simulation with an example of velocity streamlines (right). Figure inspired to [8,14].

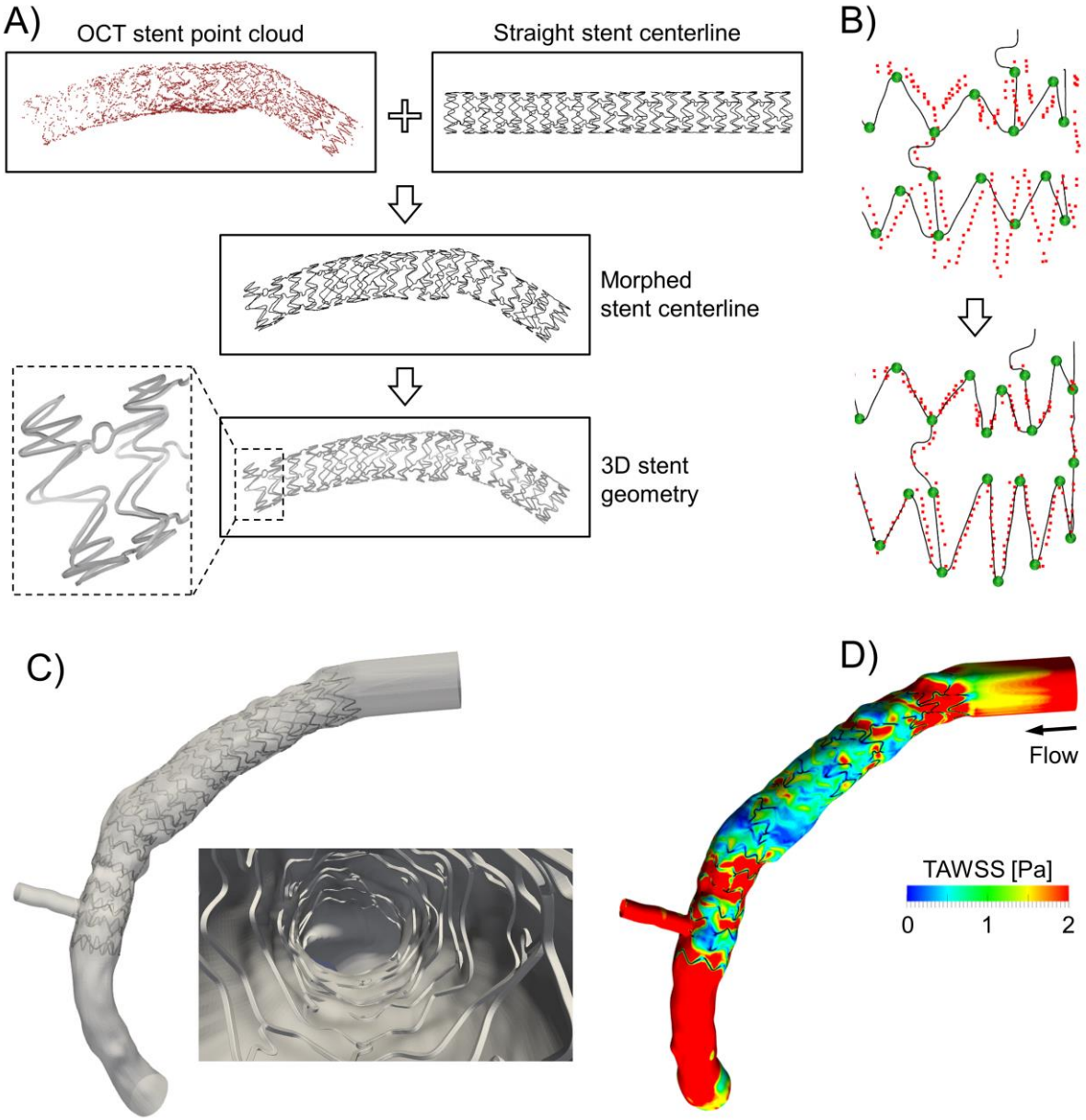

Figure 5. Morphing procedure for the creation of a patient-specific coronary artery stented model from post-operative optical coherence tomography (OCT) images for fluid dynamic analyses. A) The stent skeleton in straight expanded configuration (i.e., the straight stent centerline) is morphed on the OCT stent point-cloud to generate the deployed configuration of the stent centerline (i.e., morphed stent centerline) and subsequently the 3D stent geometry. B) Morphing of the stent centerline by using handles to minimize its distance with the OCT stent-point cloud. C) Final 3D reconstruction of the patient-specific post-operative coronary artery with detail showing the high reconstruction quality of the stent struts. D) Contour map of time-averaged wall shear stress (TAWSS) along the lumen. The region exposed to very low (< 0.4 Pa) TAWSS was confined to the stent region with percent area of

39.5%. The example case shown in this figure refers to a right coronary artery segment of a patient treated with a 3.5x28 mm Xience Prime stent (Abbott Vascular, USA) at the Institute of Cardiology, Catholic University of the Sacred Heart (Rome, Italy). The morphing procedure is described in detail in [52]. Panels A and B are reprinted with permission from [20].

Table 1. List of published studies on computational fluid dynamics simulations of patient-specific stented coronary artery models.

First author, year [reference]	Aim	Number of cases (stent platform)	Follow-up	Imaging data	Stent 3D reconstruction method	Boundary conditions	Blood model	Solver (analysis type)
Gundert et a. 2011 [12]	To develop a method for the construction of patient-specific CFD vessel models with stent	1 patient (1 open-cell and 1 closed-cell representative stent designs)	No	CT	CAD drawing	Inlet: velocity waveform from literature Outlets: three-element Windkessel representation	Newtonian fluid (μ=0.004 Pa·s), ρ=1,060 kg/m^3	Simvascular (pulsatile)
Ellwein et al. 2011 [13]	To develop a method for patient-specific coronary artery reconstruction from OCT	1 patient (Cordis Cypher)	6 months	CT + OCT	CAD drawing	Inlet: Womersley velocity profile (Q_{in} from cardiac output) Outlets: three-element Windkessel representation	Newtonian fluid (μ=0.004 Pa·s), ρ=1,060 kg/m^3	ALTAIR LesLib (pulsatile)
Chiastra et al. 2013 [8]	To study the hemodynamics of image-based coronary artery models replicating the clinical procedure of stent deployment	2 patients (Abbott Xience Prime, Medtronic Endeavor Resolute)	No	CT + angio	Stent deployment FE analysis	Inlet: parabolic velocity profile (Mean flow-rate from diameter scaling law) Outlets: flow-split based on diameter scaling law	non-Newtonian fluid (Carreau model), ρ=1,060 kg/m^3	ANSYS Fluent (pulsatile)
Gogas et al. 2013 [28]	To show the feasibility of performing a CFD analysis of patient-specific vessel including a bioresorbable scaffold	1 patient (Abbott Absorb BVS)	No	2 Angio + OCT	From OCT	NA	NA	LifeV (NA)

Papafaklis et al. 2013 [22]	To compare the relation between WSS and NIT in OCT- versus IVUS-based stented vessel models	1 patient (Abbott Absorb BVS)	6 months	2 Angio + OCT	From OCT	Inlet: flat velocity profile (Flow-rate from FCM) Outlet: 0 Pa	Newtonian fluid (μ=0.0035 Pa·s), ρ=1,050 kg/m^3	ANSYS CFX (steady-state)
Bourantas et al. 2014 [23]	To investigate the effect of WSS on neointimal formation after bioresorbable scaffold deployment	12 patients (Abbott Absorb BVS)	12 months	OCT	From OCT	Inlet: flat velocity profile (Flow-rate from FCM) Outlet: 0 Pa	Newtonian fluid (μ=0.0035 Pa·s), ρ=1,050 kg/m^3	ANSYS CFX (steady-state)
Bourantas et al. 2014 [24]	To compare OCT- versus IVUS-based model reconstructions of coronary arteries treated with bioresorbable scaffold To investigate the effect of WSS on neointimal formation	6 patients (Abbott Absorb BVS)	6 or 12 months	2 angio + OCT	From OCT	Inlet: flat velocity profile (Flow-rate from FCM) Outlet: 0 Pa	Newtonian fluid (μ=0.0035 Pa·s), ρ=1,050 kg/m^3	ANSYS CFX (steady-state)
Mortier et al. 2015 [17]	To prove the feasibility of virtually replicating a coronary stenting procedure in a patient-specific bifurcation model	1 patient (Abbott Xience Prime)	No	2 angio + IVUS	Stent deployment FE analysis	Inlet: flat velocity profile (Mean flow-rate from diameter scaling law) Outlets: flow-split based on diameter scaling law	non-Newtonian fluid (Carreau model), ρ=1,060 kg/m^3	ANSYS Fluent (pulsatile)
Chiastra et al. 2016 [18]	To develop a workflow for comparing stent designs or strategies in patient-specific anatomies	2 patients (Abbott Xience Prime, Terumo Nobori)	No	CT + OCT	Stent deployment FE analysis	Inlet: Womersley velocity profile (Mean flow-rate from cardiac output) Outlets: three-element Windkessel representation	Newtonian fluid (μ=0.004 Pa·s), ρ=1,060 kg/m^3	SimVascular (pulsatile)

Gogas et al. 2016 [29]	To show a novel 3D reconstruction method to compute the WSS at the strut level	1 patient (Abbott Absorb BVS)	No	2 angio + OCT	From OCT	NA	NA	LifeV (NA)
Thondapu et al. 2017 [25]	To compare the lumen WSS distribution post stent implantation and after 5 years follow-up	1 patient (Abbott Absorb BVS)	5 years	2 angio + OCT	From OCT	NA	non-Newtonian fluid (model = NA), ρ = NA	NA (pulsatile)
Torii et al. 2017 [26]	To compare the lumen WSS distribution in cases of underexpanded or overexapended stent	2 patients (Abbott Absorb BVS)	5 years	2 angio + OCT	From OCT	Inlet: flat velocity profile (Flow-rate from FCM) Outlet: 0 Pa	Newtonian fluid (μ = NA), ρ = NA	ANSYS Fluent (steady-state)
Migliori et al. 2018 [31]	To investigate the relation between WSS and NIT in a coronary bifurcation treated with bioresorbable scaffold	1 patient (Abbott Absorb BVS)	9 months	2 angio + OCT	From OCT	Inlet: parabolic velocity profile (Mean flow-rate from FCM) Outlet: flow-split based on diameter scaling law	non-Newtonian fluid (Carreau model), ρ=1,060 kg/m^3	ANSYS Fluent (pulsatile)
Thondapu et al. 2018 [27]	To examine immediate and long-term haemodynamic and vascular changes after bioresorbable scaffold implantation	7 patients (Abbott Absorb BVS)	5 years	2 angio + OCT	From OCT	Inlet: parabolic velocity profile Outlet: 0 Pa	non-Newtonian fluid (Quemada's model), ρ=1,060 kg/m^3, haematocrit=45%	OpenFOAM (pulsatile)
Li et al. 2018 [30]	To investigate the WSS distribution and fractional flow reserve in coronary bifurcations treated with bioresorbable scaffold	10 patients (Elixir Medical DESolve)	No	2 angio + OCT	From OCT	Inlet: velocity waveform from literature (Mean flow-rate from FCM) Outlet: NA	Newtonian fluid (μ=0.0035 Pa·s), ρ=1,050 kg/m^3	ANSYS Fluent (pulsatile)

Table legend: CT – computed tomography; Angio – angiography; IVUS – intravascular ultrasound; OCT – optical coherence tomography; FE – finite element; CFD – computational fluid dynamics; Q_{in}= inlet flow-rate; WSS – wall shear stress; NIT – neointimal thickening; FCM – frame count method; μ – dynamic viscosity; ρ – density; NA – not available.